Medical Engineering and Physics 107 (2022) 103874

Contents lists available at ScienceDirect

Medical Engineering and Physics

journal homepage: www.elsevier.com/locate/medengphy

Flows of healthy and hardened RBC suspensions through a micropillar array

Antonios Stathoulopoulos [a], Andreas Passos [a,c], Stavroula Balabani [a,b,*]

[a] FluME, Department of Mechanical Engineering, University College London (UCL), London, WC1E 7JE, United Kingdom
[b] Wellcome/EPSRC Centre for Interventional and Surgical Sciences, University College London (UCL), London, United Kingdom
[c] Department of Mechanical Engineering and Material Science Engineering, Cyprus University of Technology, Limassol, Cyprus

ARTICLE INFO

Keywords:
Blood micro flows
RBC deformability
Micropillar arrays
MicroPIV

ABSTRACT

Red blood cell (RBC) deformability is an important haemorheological factor; it is impaired in many pathologies leading to microvascular complications. Several microfluidic platforms have been utilized to examine the role of deformability in RBC flows but their geometries tend to be simplified. In the present study, we extend our previous work on healthy RBC flows in micropillar arrays [1] to probe the effect of impaired RBC deformability on the velocity and haematocrit distributions in microscale RBC flows. Healthy and artificially hardened RBC suspensions at 25% haematocrit were perfused through the micropillar array at various flow rates and imaged. RBC velocities were determined by Particle Image Velocimetry (PIV) and haematocrit distributions were inferred from the image intensity distributions. The pillars divide the flow into two distinct RBC streams separated by a cell-depleted region along the centreline and in the rear/front stagnation points. RBC deformability was not found to significantly affect the velocity distributions; the shape of the velocity profiles in the interstitial space remained the same for healthy and hardened RBCs. Time-averaged and spatiotemporal intensity distributions, however, reveal differences in the dynamics and local distributions of healthy and hardened cells; hardened cells appear to enter the cell-depleted regions more frequently and their interstitial distributions are more uniform. The study highlights the importance of local RBC distributions and the impact of RBC deformability on cell transport in complex microscale flows.

1. Introduction

Blood is a dense suspension of soft particles the majority of which are RBCs. RBCs play a key role in human physiology; their highly deformable structure allows them to pass through narrow vessels in the capillary network (typically 5–6 μm in diameter) delivering oxygen and nutrients to tissues [2]. The particulate nature of blood gives rise to interesting phenomena in the microcirculation. For example, RBCs tend to migrate laterally due to shear and interactions with the vessel walls [3,4]; this effect is counteracted by a diffusion-like motion induced by the collisions between cells [5]. Combined with the complex topology of microvascular networks, these shear-induced effects lead to heterogeneous cell (haematocrit) distributions and well-known phenomena such as 'plasma skimming' [6,7]. These phenomena are highly dependant on the biomechanical properties of RBCs, particularly RBC deformability. The latter is impaired in a number of pathologies, such as malaria [8], sickle cell disease [9], diabetes [10] as well as sepsis [11,12] altering microhemodynamics, increasing blood flow resistance in the microvasculature [13,14] and compromising tissue perfusion [15,16].

Microfluidics has enabled researchers to study such phenomena in a systematic manner [17,18]. A number of in vitro studies on microscale blood flows in straight [4,19–22] and bifurcating microchannel geometries [23–25] have shed light on flow partitioning and RBC biomechanics. Recently, artificial microfluidic networks have been developed in order to elucidate blood flow in more realistic microcirculation geometries [26,27].

In many organs, microvasculature can deviate from straight or bifurcating geometries [28–30] the majority of published microfluidic studies emulate. For example, in the lungs [31–33] or the human placenta [34,35] blood flows past structures (e.g. alveoli/villi) resembling pillar arrays and exhibiting more complex flow kinematics. While microfluidic pillar arrays have commonly been employed to separate cells based on deformability [36–38] or size [39] relatively little work has been done on the transport of RBC suspensions through such

* Corresponding author.
E-mail address: s.balabani@ucl.ac.uk (S. Balabani).

https://doi.org/10.1016/j.medengphy.2022.103874
Received 20 May 2022; Received in revised form 29 July 2022; Accepted 9 August 2022
Available online 10 August 2022

geometries. Stauber et al. [40] employed a microchannel with a dense array of posts to mimic alveolar capillary networks and studied the motion of RBCs therein. Gomez Bardon et al. [1] used microfluidic devices with pillar arrays to study the blood flow past oxygenator fibers with a view to improve modelling and design of extracorporeal artificial lungs for intensive care therapies. They examined the heterogeneous distribution of RBCs in different pillar array arrangements and their implications for oxygen delivery and device performance. A more sophisticated lab-on-a-chip approach to mimic alveoli has been recently proposed by Huang et al. [33], making use of a hydrogel to create the pores of the alveolar sacs and epithelial cells to line the inner environment of the sacs and provide a more realistic approach for in vitro studies. Microfluidic devices featuring successive rows of circular [41] or square [42] pillar arrays have recently been reported, mimicking the blood filtering function of the spleen, removing aged or infected RBCs from the body by passing them through interendothelial slits.

The blood flow through micropillar arrays has also been studied numerically in the context of oxygen transfer in the human placenta [43, 44] or deterministic lateral displacement (DLD) devices with cylindrical [45,46] or non circular pillars [47] in order to elucidate RBC trajectories as a function of parameters such as haematocrit (i.e. RBC concentration) or deformability and optimize separation.

Motivated by our previous work on RBC flows in bifurcating geometries and on the role of RBC deformability on microchannel flows [22], we extend the work of Gomez Bardon et al. [1] to elucidate the effect of deformability on the transport of dense suspensions of RBCs in the interstitial space of a microfluidic pillar array. The flow therein exhibits interesting kinematics featuring curvature, converging and diverging flow regions as well as stagnation points. Hence, it provides an opportunity to explore RBC transport and interactions in more complex domains. Healthy and artificially hardened RBC suspensions at 25% haematocrit were perfused through the micropillar array and imaged using microscopy as in our previous studies [22,23,48]. Velocity and cell distributions as well as spatiotemporal maps were extracted in order to analyse the influence of impaired RBC deformability on cell transport.

2. Experimental methods

2.1. Blood sample preparation

Blood samples were obtained from consenting donors via venepuncture and mixed with $1.8 mg ml^{-1}$ EDTA to prevent coagulation. Red blood cells (RBCs) were separated from whole blood through centrifugation, washed twice in phosphate buffered saline (PBS) and resuspended in PBS at a haematocrit (Ht) of 25% to prevent aggregation during measurements. RBC deformability was altered by incubating the cells in glutaraldehyde (GA) solution at 0.08% concentration for 15*min* as described in Passos et al. [22]. All samples were used within 4 h after their collection and according to the protocol approved by the South East London NHS Research Ethics Committee (Reference: 10/H0804/21). Measurements reported herein were taken with samples from the same donor in order to avoid inter donor variation in RBC properties.

2.2. Microfluidic channel

The microfluidic geometry comprised an array of six circular pillars similar to one of the geometries employed in Gomez Bardon et al. [1]. The pillars had a diameter (D) of 380 μm and were spaced at 1.58D. Half pillars were placed on the side of the channel to emulate an infinite rotated square array (see inset of Fig. 1). The minimum gap (d) between these staggered pillars was 50 μm. The channel height (h) was 40 μm. Microchannels were fabricated in PDMS using standard soft lithography techniques and bonded on microscope glass slides using oxygen plasma treatment.

2.3. Experimental setup

A schematic of the experimental setup is shown in Fig. 1. The microchannel was placed on the stage of an inverted microscope (Leica DM ILM, Germany) and perfused with the RBC suspensions using a bespoke pneumatic microfluidic flow controller as described in

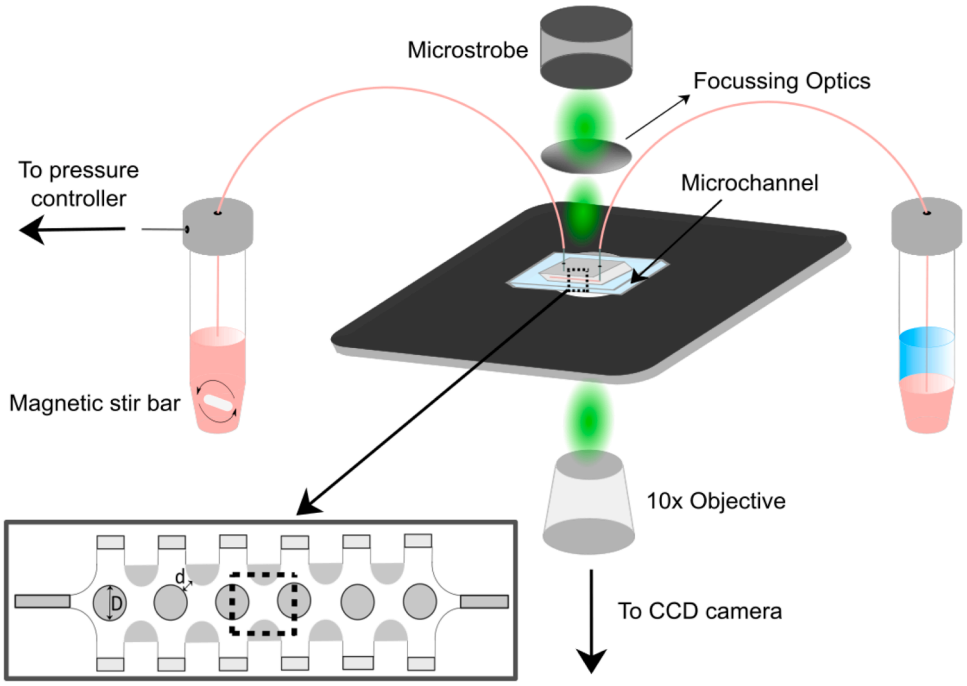

Fig. 1. Schematic representation of the experimental setup. The blood sample is stirred continuously in between measurements using a magnetic stirrer to avoid sedimentation and aggregation of the cells and perfused via a pressure controller. The inset shows the microfluidic geometry and the measurement region. (For interpretation of the references to colour in this figure legend, the reader is referred to the web version of this article.)

Sherwood et al. [25]. The flow was illuminated with a green LED microstrobe and images were acquired at the midplane of the channel and between the 3rd and 4th micropillar (see inset of Fig. 1) using a Charged Coupled Device (CCD) camera (Hamamatsu, C8484–05C, Japan) and a 10x objective (NA=0.25). A frame rate of 6*Hz* was used and 120 images were acquired. The time interval between image pairs was adjusted between$0.5 - 4ms$ in order for the maximum RBC displacement to be less than a quarter of the interrogation width during the PIV analysis.

Both perfusion and imaging were controlled using a custom-made LabVIEW (National Instruments, USA) code as described in our previous work [23,25]. The experiments were carried out at room temperature. To ensure even distribution of the cells in the tubing and the microchannel region, the samples were gently stirred and perfused at a high flow rate prior to each measurement.

2.4. Micro particle image velocimetry (microPIV)

The images were cropped in order to analyse the flow in a cell of the rotated square array, i.e. the space between four neighbouring pillars as shown in Fig. 2(a), using MATLAB (MathWorks, USA). MicroPIV processing was implemented in PIVlab [49] to extract the velocity field using ensemble correlation with 3 passes and a final interrogation window (IW) size of $8px x 8px$ and 50% overlap. The normalised median test was used to identify invalid vectors [50] (less than 0.1%) and outliers were replaced by the median of the surrounding vectors. The image resolution was $0.65\mu m px^{-1}$ and the spatial resolution of the measurements was $2.6\mu m$ (i.e. vector spacing). Due to pixel diffraction closer to the pillar wall, the first experimental point is located 8 pixels from the wall while the finite size of the RBCs allows them to roll along the channel wall.

A typical vector field is shown in Fig. 2(b). Velocity profiles were extracted in selected locations between the pillars as illustrated in Fig. 2 (c) as well as in the minimum gaps between the pillars. These were calculated by axially averaging the measured velocities within the narrow regions of interest (ROIs) ($8px$ in width which is approximately 0.01D) indicated by the red lines to minimize the error, i.e. the standard deviation of the velocity profiles within the ROI. Spline interpolation was used to fit the velocity data and smooth the resulting velocity profiles.

The depth of correlation in the current microPIV setup is expected to be larger than the channel depth resulting in an underestimation of the measured velocity values due to the out-of-plane motion of RBCs [51]. Poelma et al. [52] suggested a correction factor a, which is equal to 1.5 for the current setup. In this study all reported velocities (u^*, U^*) were normalised in order to facilitate comparisons and mitigate the effects of the depth of correlation. The flow rates (ranging from 1 to 3 μL/min) are estimated by integrating the measured velocity profiles at the inlets and outlets of the domain, taken at the narrowest RBC passages between successive rows; i.e. $Q=U_{mean}{}^*A$, where U_{mean} is the mean velocity corrected by the scaling factor α and A the cross-sectional area (equal to 50 μm x 40 μm). U_{mean} is calculated by trapezoidal numerical integration of the profiles shown in Figs. 3(c) and **(d).** The corresponding Reynolds numbers were lower than 1 and hence inertia effects can be neglected. The difference between the inlet and outlet flow rates was used as an indication of the velocity measurement error. This was found to range between 3 and 4% for normal RBCs and 0.7–2.3% for hardened ones.

2.5. Image intensity distributions

The time-averaged intensity distribution was used as a measure of the local RBC concentration; i.e. it is assumed that at each location the intensity of the time-averaged image is inversely proportional to the local haematocrit [53]. Fig. 2(c) shows such a typical mean image intensity map computed from 120 RBC images. The mean intensity values were normalised by the maximum image intensity in the area outside of the channel (I_{max}), i.e. $I^* = I_{raw}/I_{max}$ and expressed in terms of $1 - I^*$ so that darker regions correspond to higher haematocrit. Normalised intensity profiles I^* were computed in the same locations and ROIs as the velocity profiles for comparisons.

Spatio-temporal intensity maps were also generated in regions close to the stagnation points and along the wake centreline in order to compare the dynamics of healthy and hardened cells. These are produced by averaging the normalised instantaneous image intensity in thin strips of $30px$ x $342px$ in the x^* direction as in Cagney et al. [54]. The root-mean-square (RMS) level of each flow map is also calculated along the y^* direction as a measure of cell dispersion.

3. Results

3.1. Velocity profiles

The vector field in Fig. 2(b) and the contours of the axial velocity component (Fig. 3(a)) illustrate some typical features of flow inside a staggered pin array. Maximum velocities are located in the minimum gaps between successive row pillars, as the flow accelerates in this

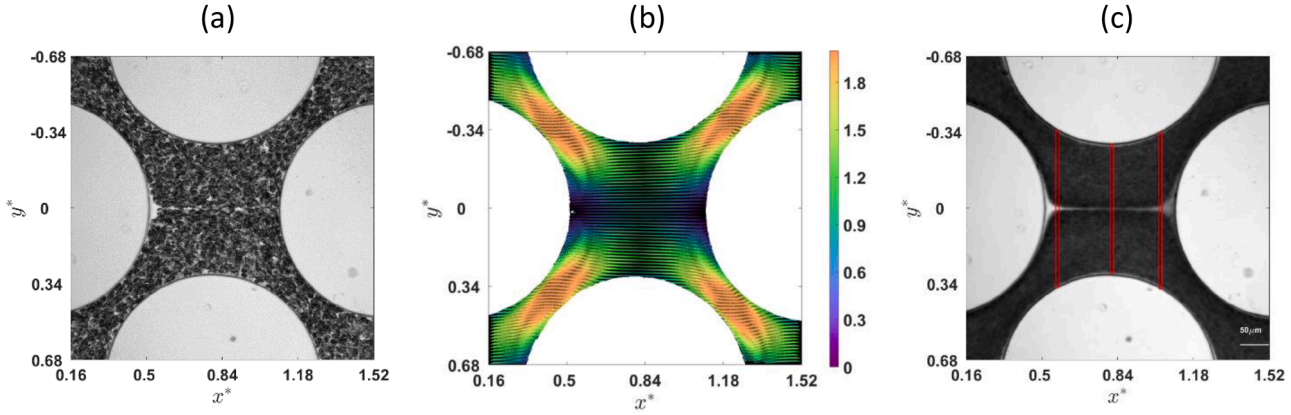

Fig. 2. (a) Sample instantaneous image of RBCs flowing in the interstitial space of the array. Blood enters through the inlets on the left side of the figure and exits from the gaps on the right. (b) Typical velocity vector field obtained by microPIV processing. Velocities (U^*) are normalised by the mean axial velocity across the interstitial space of the geometry. The coordinates are normalised by the diameter of the pillar D, $x^* = x/D$ and $y^* = y/D$. The coordinate system is defined such that the origin (0,0) is in the centre of the upstream pillar. (c) Time-averaged image of the flowing RBCs over a period of 10 s at a flow rate of 2.05 μL min−1. Solid red lines indicate selected locations and ROIs where velocity profiles were extracted. (For interpretation of the references to colour in this figure legend, the reader is referred to the web version of this article.)

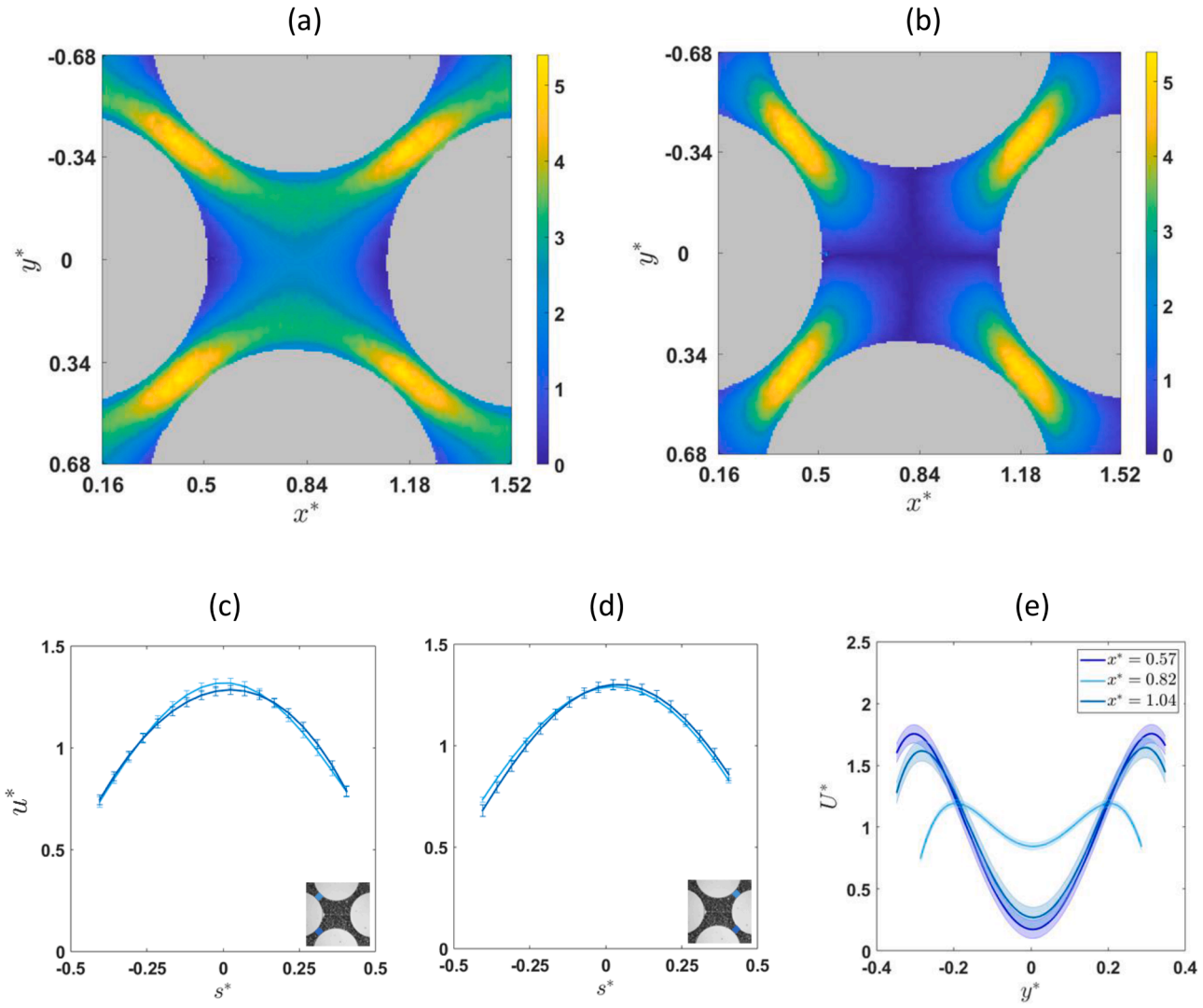

Fig. 3. Contours of (a) axial and (b) transverse velocities of the flow domain expressed in mm/s. Normalised velocity profiles of healthy RBCs in the gap flows at the two inlets (c) and outlets (d) of the domain as indicated in the inset images and (e) at selected axial x^*-positions (the normalised axial velocities are illustrated) in the interstitial region between the pillars. Lines are polynomial fits to the experimental data, error bars and shaded regions indicate one standard deviation. The coordinates are normalised by the gap width, d, for the inlet/outlet flows ($s^* = s/d$) and the pillar diameter, D, ($y^* = y/D$) in the interstitial space. u^* denotes velocities normalised by the mean gap flow velocity in each branch and U^* normalised by the mean flow velocity across the interstitial space.

region, whereas the interstitial region is characterised by lower axial mean velocities, especially around the rear and front stagnation points and along the centreline. The transverse mean velocities (Fig. 3(b)) attain zero values along the centreline ($y^* = 0$) indicating that the cells, on average, do not cross the centreline.

These features can be seen in more detail in Fig. 3(c)-(e) comparing selected velocity profiles of healthy RBC suspensions in the measured flow domain. The profiles at the two inlets and outlets match (no statistically significant difference between the profiles was identified through t-test), implying that there is an equal split of the flow upon impinging the upstream and downstream pillars respectively.

Fig. 3(e) illustrates the flow development in the interstitial space (wake of the upstream pillar) by showing velocity profiles at selected axial locations namely near the rear ($x^* = 0.57$)and front stagnation points ($x^* = 1.04$)of upstream and downstream pillars respectively, and in the middle of the interstitial space ($x^* = 0.82$). The stagnation flow profiles exhibit similar behaviour; they are characterised by V shape profiles with a pronounced velocity deficit near the centreline and high velocities near the side pillars due to the fast incoming/outgoing flow streams respectively. In the middle of the interstitial space ($x^* = 0.82$), the velocity profile exhibits a double-peak shape indicating some flow recovery; velocities remain low along the centreline and are higher in the flow lanes either side, but the velocity gradients are less steep compared to the profiles in the proximity of upstream/ downstream pillars.

To examine the influence of RBC deformability on the flow distribution inside the array, we compare the streamline patterns and selected velocity profiles for normal and hardened RBCs. The streamlines for healthy (i.e. Fig. 4(a)) and hardened RBCs (i.e. Fig. 4(b)) appear similar; no notable differences can be observed apart from the vicinity of the stagnation regions, as also evidenced from the velocity profiles (Figs. 4 (c-g)).

Figs. 4(c) and 4(d) compare selected gap velocity profiles - the locations are indicated by the insets. Although the hardened cells appear to flow slightly faster in the gaps (especially in the outlets, i.e. Fig. 4(d)) compared to healthy RBCs (i.e. their velocity profiles appear sharper), the observed differences are not statistically significant. Similar trends were observed in the velocity profiles in Figs. 4(e), 4(f) and 4(g) calculated at three distinct interstitial locations as indicated in Fig. 2(c).

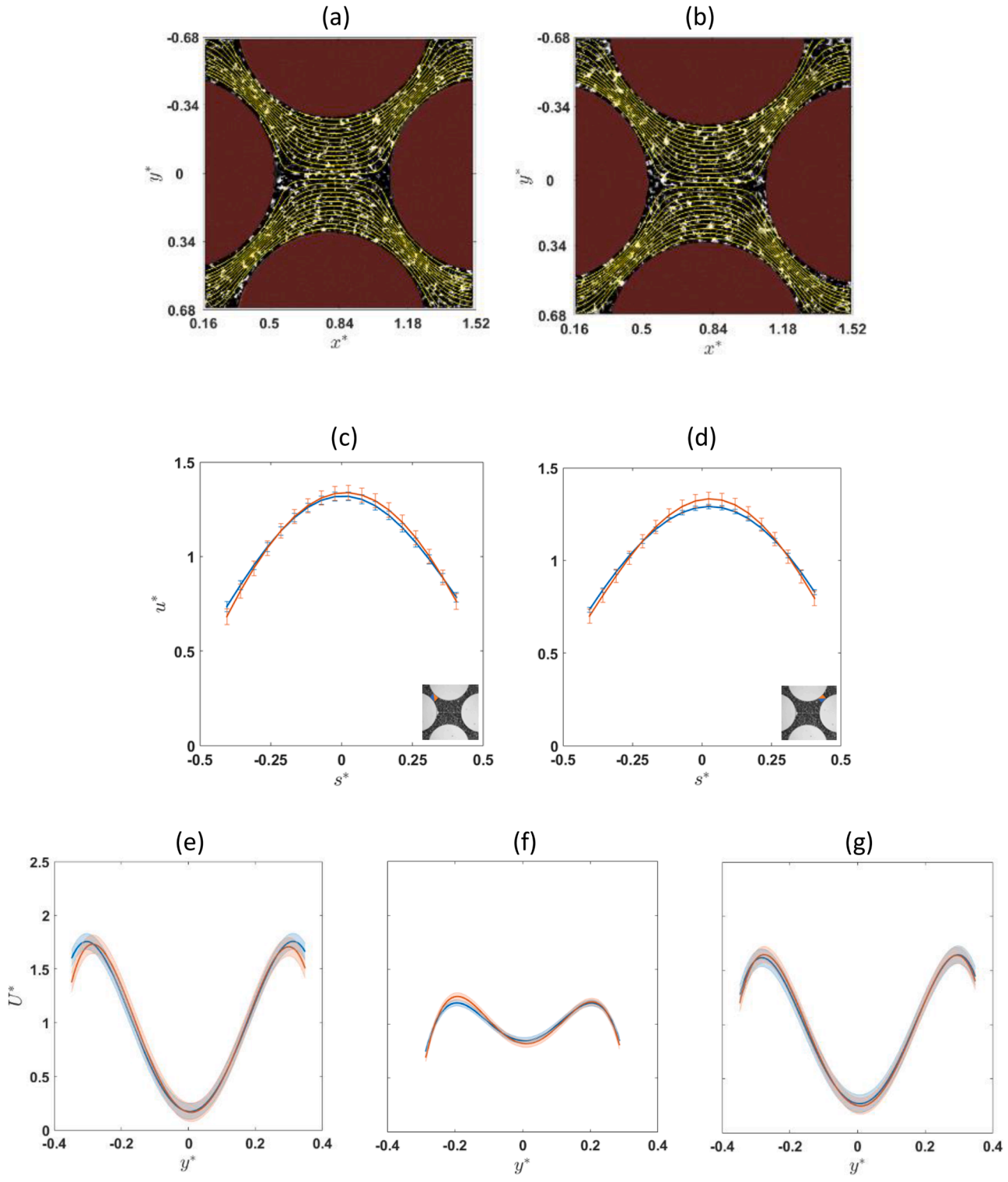

Fig. 4. Typical RBC flow streamlines for (a) healthy and (b) hardened RBCs and a flowrate of 2.05 μL min−1. Comparison of normalised RBC velocity profiles for healthy (blue) and hardened (orange) RBCs; indicative inlet and outlet gap flows in selected locations shown in the inset images (c-d) and at the interstitial space between the pillars (e) $x^* = 0.57$(f) $x^* = 0.82$ (g) $x^* = 1.04$. Lines are polynomial fits and error bars and shaded regions showing the standard deviation of the experimental data. s^*, y^*, u^*, U^* are defined in Fig. 3. (For interpretation of the references to colour in this figure legend, the reader is referred to the web version of this article.)

3.2. Intensity distributions

Fig. 5 shows normalized time-stacks of 120 images for healthy and stiffened RBCs which provide an indication of the local RBC distribution in the array. A cell depleted zone is evident along the centreline $y^* = 0$, indicating that the two RBC streams emanating from the upstream pillar and entering the flow domain do not mix. Cell depletion regions are also identified in the vicinity of the rear and front stagnation points of the upstream/downstream pillars respectively, and near the walls of side pillars as expected. A closer look at the distributions shows distinct

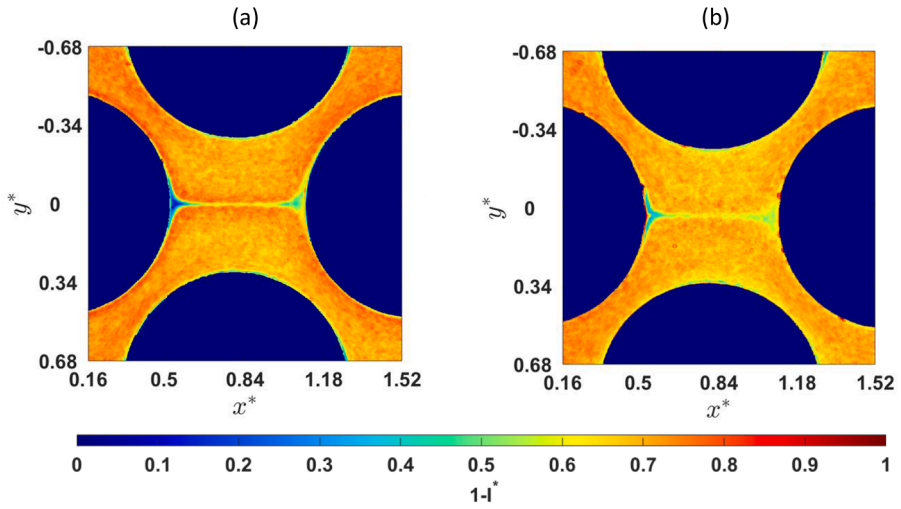

Fig. 5. Time-averaged image intensity distribution (1-I^*) indicating local RBC concentration in the array at a flow rate of 2.05 μL min−1. (a) healthy RBCs, (b) hardened RBCs.

differences between healthy and hardened cells. The hardened cells seem to be able to enter the cell-depleted stagnation regions, cross the centreline and to be more uniformly distributed on both sides of the centreline (Fig. 5(b)). Healthy cells on the other hand seem to concentrate on either side of the cell depletion regions along the centreline $y^* = 0$; this leads to a higher cell concentration along the surface of the downstream pillar (the accelerating part of the flow (Fig. 5(a)).

The differences between healthy and hardened RBC distributions are further illustrated in Fig. 6 showing normalized intensity profiles at the interstitial locations indicated in Fig. 2(c). Across the rear stagnation point (i.e. Fig. 6(a)) the distribution of the healthy cells is characterized by a sharp dip in the centerline indicating the absence of cells in the stagnation region and a peak concentration on either side of the centerline. On the other hand, the hardened cells show a more uniform distribution on either side of the centerline and higher concentration in the rear stagnation point implying that the hardened cells are able to penetrate the stagnation region. Similar trends but with a less prominent depletion at$y^* = 0$ can be seen in the mid axial station between the two successive pillars ($x^* = 0.82$), Fig. 6(b). In the vicinity of the downstream pillar (Fig. 6(c)) the distributions of the healthy and hardened cells appear similar with the exception of the front stagnation point where healthy cells exhibit a distinct and sharper dip in concentration compared to hardened cells. Unlike the velocity profiles, the observed differences in the intensity maps between healthy and hardened cells in Fig 6 are found to be statistically significant using *t*-test analysis.

In order to examine the different cell dynamics and hydrodynamic interactions between healthy and hardened cells (i.e. Figs. 5 and 6), we generate spatio-temporal maps in three distinct locations as shown in Fig. 7.

The maps in Fig. 7 illustrate the most pronounced tendency of the hardened RBCs to move in and out of the stagnation regions and cross the centreline compared to the healthy cells. This is also reflected in the rms intensity profiles (Figs. 7(d) and 7(h)): the rms intensity of the hardened RBC flow maps fluctuates more around the centreline due to the cells entering the cell-depleted regions more often. An interesting double peak can be observed behind the rear stagnation point.

The thickness of the cell-depleted layer ($\delta_{centerline}$) along the centreline was estimated from binarized time-averaged images (Fig. 8(a)) and plotted for healthy and hardened cells in Fig. 8(b). A continuous cell depletion region is evident along the centreline for healthy cells whereas the one for hardened cells appears intermittent. The enhanced tendency of hardened RBCs to enter the depleted region in comparison with healthy RBCs is also evident from the variation of $\delta_{centerline}$ across x^* in agreement with Figs. 7(b) and 7(f).

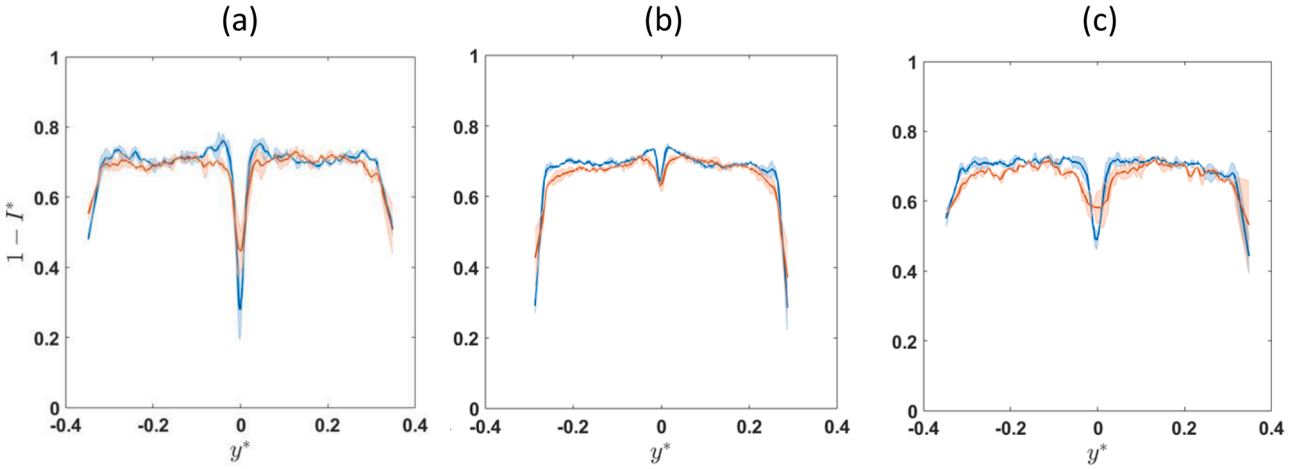

Fig. 6. Comparison between healthy and hardened cell distributions; intensity profiles 1-I^* at (a) $x^* = 0.57$(b) $x^* = 0.82$ (c) $x^* = 1.04$. Lines show spline fits to the data and shaded regions show one standard deviation. Blue denotes healthy cells and orange hardened ones.

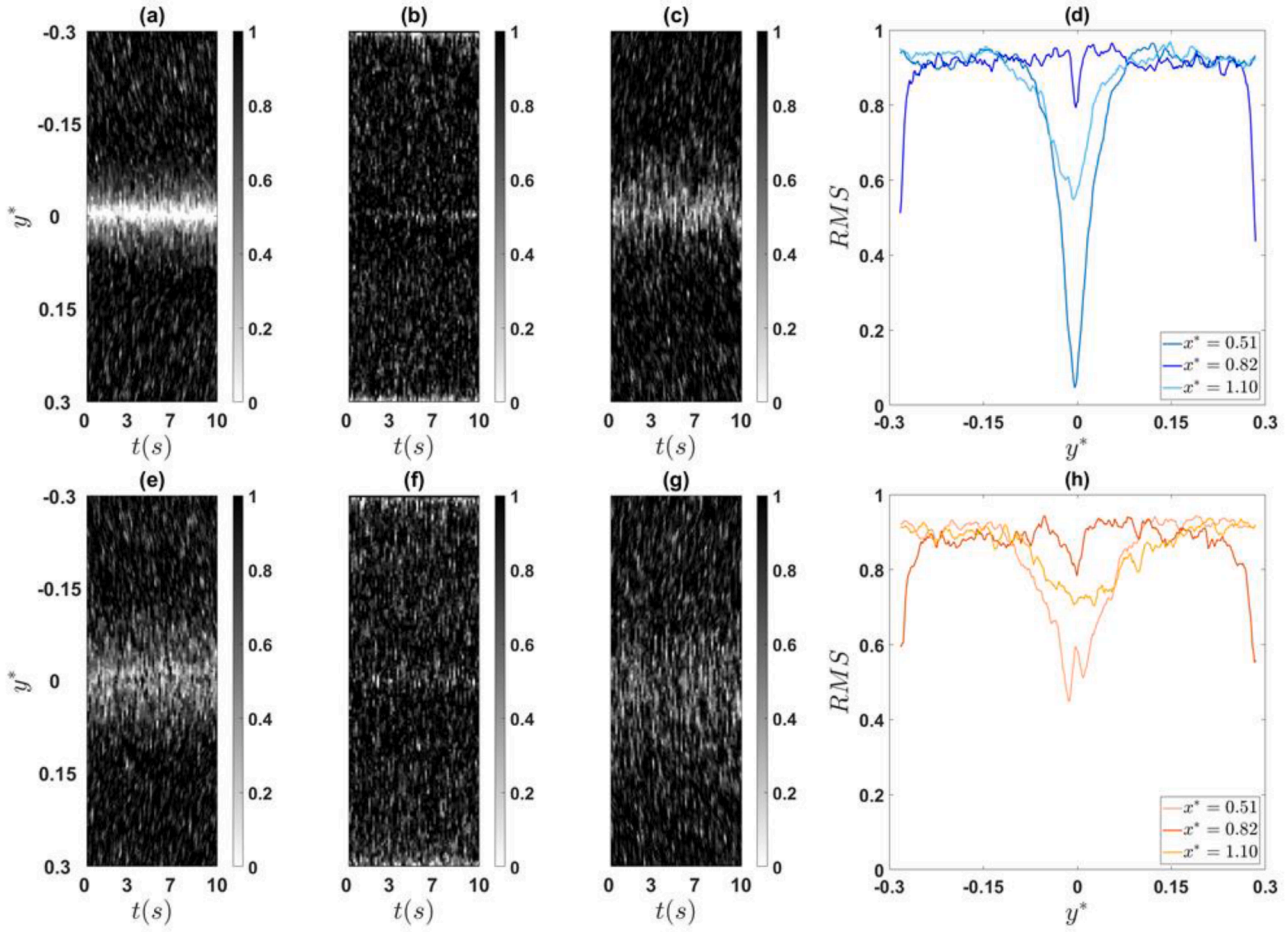

Fig. 7. Spatio-temporal intensity maps (1-I^*) for healthy ((a),(b),(c)) and hardened RBCs ((e),(f),(g)) at a flow rate of 1.37 μL min−1 and three distinct locations, (a, e) $x^* = 0.51$(b,f) $x^* = 0.82$ (c,g) $x^* = 1.10$; (d),(h) Root mean square of the flow maps across the channel width for healthy and hardened cells, respectively.

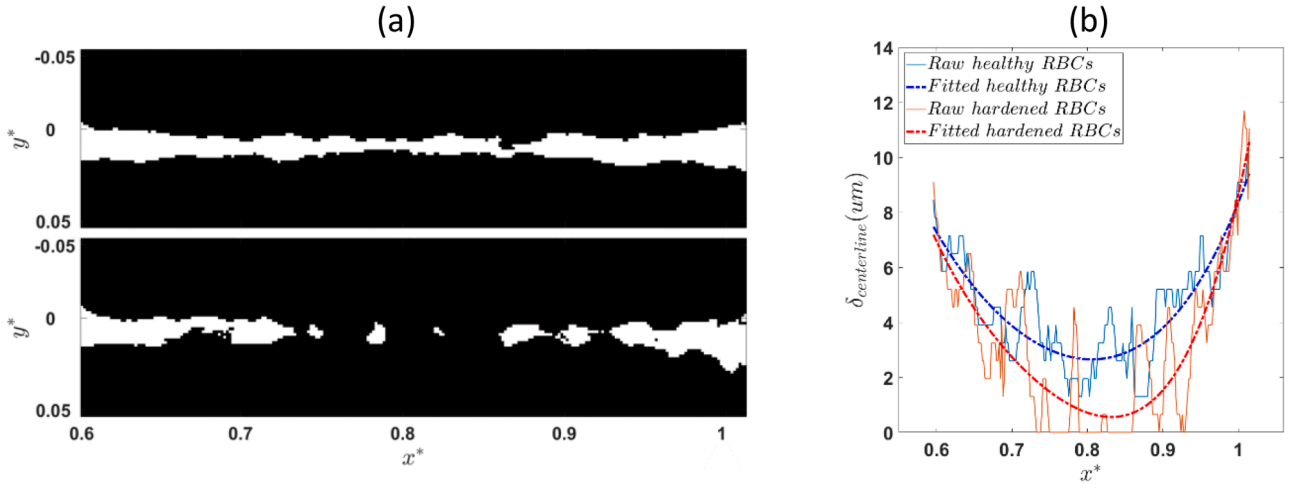

Fig. 8. (a) Binarised time-averaged images along the centerline for healthy (top panel) and hardened (bottom panel) RBCs at a flow rate of 2.05 μL min−1. (b) Width ($\delta_{centerline}$) of the depletion zone along the centerline for healthy (solid blue) and hardened (orange) RBC suspensions; fitting curves for each data set (dotted lines) are drawn to guide the eye. (For interpretation of the references to colour in this figure legend, the reader is referred to the web version of this article.)

4. Discussion

4.1. Flow patterns and RBC distributions

RBCs experience a mix of kinematics as they flow past the pillars in the array; they encounter regions of contracting flows in the minimum gaps between neighbouring pillars-where they accelerate producing velocity profiles that appear almost parabolic (Figs 3(c) and 3(d))- and of expanding flow in the interstitial space (Fig. 3(e)). The presence of stagnation points, changes in the flow cross-sectional area and the self-

organization of the cells therein result in symmetric axial velocity profiles that exhibit double peaks. In the middle of the interstitial space ($x^* = 0.82$)-where the cross-section is the smallest- maximum axial velocities are recorded halfway between the centreline and the pillar walls (Figs. 3(e) and 4(f)); the non-uniform character of the profiles is more pronounced in the vicinity of the stagnation points ($x^* = 0.57 \text{and} x^* = 1.04$); higher peak values away from the centreline and near zero velocities on the centreline are evident (Fig. 3(e)). The transverse velocity maps (Fig. 3(b)) indicate negligible momentum transfer across the centreline; thus, partitioning of the flow by the pillars results in a 'stratified' flow in the interstitial space, whereby the cells flow in two distinct lanes separated by the centreline.

Double peaked velocity profiles have been previously reported for dilute (1%- 5%) RBC flows in a sudden contraction-expansion [55]; these were obtained by density weighted averaging over the channel depth and were attributed to an RBC focusing effect resulting from the balance between wall-lift and shear-gradient forces. Such focusing (off centre RBC density peaks) has also been reported for dilute RBC flow in a microchannel in the absence of inertia [56]. This effect was the result of lateral migration and weakened with feed haematocrit and channel length.

Lateral migration is expected to play a role in the spatial organisation of the cells in the interstitial space of the array studied here. The cells are expected to move away from both the centreline and the pillar walls due to the shear gradients in these regions (shear-induced migration) as well as the wall lift induced by the pillars. As the suspension is dense, collisions between the cells (shear-induced diffusion) are expected to counteract these effects. The intensity distributions in Fig. 5 provide evidence of the complex RBC dynamics in the flow under investigation. The most striking feature is the cell-depleted region along $y^* = 0$ (Fig. 5(a)); it emanates from the rear stagnation point of the upstream pillar and extends up to the front stagnation point of the downstream pillar, dividing the flow into two streams. An accumulation of healthy cells on either side of the centreline can be discerned in the intensity profiles (Fig. 6); this is more prominent in the vicinity of the rear stagnation point, a region of negligible velocities that the cells seem to be unable to penetrate.

The heterogeneity in the spatial organisation of RBCs in micropillar flows has been illustrated for various array geometries, including the one studied here, previously [40]. Cell depletion regions along the centreline of pillars were observed; the latter persisted throughout the arrays and on exiting flows and their extent depended on the feed haematocrit. It should be noted that inertia was non negligible in that study as the intention was to mimic fibre oxygenators that typically operate at higher Reynolds numbers (*Re*).

The observed RBC distributions can be attributed to the short length between successive pillars which does not allow sufficient time for RBCs to disperse radially. This together with the initial distribution of cells upon encountering the inner pillars result in complex and fairly persistent patterns in the array. The gradient diffusivity of healthy cells in the present study (following [4]) is estimated to be in the order of 10^{-6} cm^2/s which implies a mean cell displacement of approximately 2.5 μm during their transport through the interstitial space. Despite the low flow rates used in the present study, convective transport appears to be more dominant as the ratio of advection time to diffusion transport time for RBCs to travel along the interstitial space between the micropillars is found to be of the order of $10^{-4} << 1$, following the analysis of Mantegazza et al. [57].

Short lengths for the suspension distribution to fully develop have been identified as one of the reasons for the heterogeneous flow partitioning observed in sequential bifurcations [57]. The length required to restore the haematocrit profiles from a focusing effect has been found to exceed 23 hydraulic diameters for dilute suspensions in a rectangular microchannel and to be dependent on aspect ratio [56]. A length of 3.5 mm has been estimated by Mantegazza et al. [57] for a channel of 10 μm width and 10% suspensions whereas Losserand et al. [58] found that a distance of 200 μm is needed for RBCs to pass through a 2 μm CFL and a 150 μm to obtain equilibration in 30% suspensions flowing in channels 5 μm wide. In the present study, the equilibration time due to shear-induced diffusion for healthy RBCs is 73.55 s for the highest flowrate employed and the corresponding length is approximately 440 mm.

While the time-averaged profiles and the velocity maps imply no mixing between the two RBC streams entering the interstitial space, the spatio-temporal maps (Fig. 7) indicate that the cells occasionally cross the centreline; the effect is more pronounced at the mid axial plane (Fig. 7(b)) and near the front stagnation point of the downstream pillar where the flow partitions again. However, this is not the case for the rear stagnation point (Fig. 7(a)) where a persistent cell depletion region can be detected throughout the duration of the measurement.

The RBC dynamics at the front stagnation point might explain the close (statistically) match between the two outlet (and inlet) velocity profiles (Figs. 3(c) and 3(d)) and agrees with reports in the literature regarding flow preservation in diverging bifurcations [59]. Schmid et al. [59] numerically demonstrated that despite the global heterogeneity in microvascular networks, local RBC dynamics regulate the flow ratio in diverging bifurcations with RBCs distributing so that to balance outflow velocities. The same observations are also documented in the experimental work of Mantegazza et al. [60], where a honeycomb network is used to replicate complex microvasculature. They report that in low-flow conditions, there is a well-balanced distribution of the flow when it reaches a bifurcation point and it is primarily affected by the dynamics of RBCs. A low degree of lateral displacement has also been reported by Stauber et al. [40] for RBC suspension flows in highly confined micropillar arrays; they demonstrated that RBCs tend to follow single longitudinal pathways with limited crossing between them which agrees with the present study.

4.2. Role of RBC deformability

We have shown previously [22] that hardened RBCs produce sharper velocity profiles in microchannels with a 50 μm width. This was attributed to the effects of hardening on cell distribution and the shear thinning nature of the suspension. Surprisingly, no statistically significant differences between healthy and hardened RBC velocity profiles are observed in this study (Fig. 4) despite RBCs hardened using the same protocol, in agreement with the study of Abay et al. [55] for dilute RBC suspensions in an expanding flow. Despite the similarity in flow velocities, altered cell membrane properties appear to have an impact on the distribution of cells; unlike healthy RBCs, hardened ones show an ability to penetrate low velocity regions, a trend also reported by Abay et al. [55]. This is illustrated in the intensity distributions (Figs. 5 and 6) but even more so in the spatio-temporal RBC maps in the vicinity of the stagnation points (Figs. 7(e) and 7(g)), which provide a striking example of the differences between the dynamics of healthy and hardened cells.

RBC deformability is a key determinant of individual cell motion, the forces acting upon the cells as well as cell-cell interactions. Deformability is associated with tank treading motion and enhances the lateral migration of RBCs [61] by promoting wall lift forces [62–65]. Hardened cells exhibit a tumbling behaviour [66,67] limiting their inward migration towards the flow centre [5,68].

In crowded environments, such as in a 25% Ht suspension, RBC dynamics are likely to be dominated by cell-cell interactions, modifying cell distributions accordingly [58,68]. While collisions between healthy RBCs result in cell deformation which helps them to maintain their original positions, collisions between hardened RBCs result in greater cell displacement post-collision [69,70]. As a result, hardened cells exhibit an enhanced collision induced drift allowing them to cross streamlines and enter stagnated flow regions [71,72] producing an intermittent cell-depleted region along $y^* = 0$(i.e.Fig. 8(b)) and more uniform distributions across the interstitial space compared to healthy RBCs (Figs. 6 and 7(e) to 7(h)).

4.3. Study limitations

In the present study RBCs were hardened using glutaraldehyde, a commonly employed agent. Based on our previous work [22], a 0.08% glutaraldehyde solution and a 25% haematocrit concentration of both suspensions were deemed sufficient to elucidate the differences between healthy and hardened RBCs, in terms of velocity and cell distributions at the microscale for a narrow - but physiologically relevant - range of flow rates. A wider range of feed haematocrits and higher, finite *Re* have been studied in our previous work [1] for healthy cells and similar heterogeneous haematocrit distributions observed.

A high aspect ratio channel was employed. Measurements were limited to the middle plane but the shear gradients are expected to be higher along the depth of the channel affecting both the measured flow field and the distribution of RBCs as illustrated by Abay et al. [55]. The measured flow domain is considered representative of the flow deep in micropillar arrays; however, half pillars have been added on the end walls to mimic an infinite array, a common practice in experimental studies of flows in cylinder arrays [73,74] which might have a slight influence on the measured flow fields.

5. Conclusions

The role of RBC deformability in the transport of dense human RBC suspensions in a micropillar array was examined experimentally. Two distinct RBC streams on either side of the centreline, originating from the pillar-induced flow partitioning, characterised the interstitial space flow. A non-uniform cell distribution marked by pronounced cell depleted regions in the stagnation points and along the centreline was evident.

The measured velocity profiles showed no statistically significant differences between healthy and hardened RBCs, unlike our previous studies with straight microchannels [22]. However, distinct differences were observed in the spatial organisation of the cells. Impaired cell deformability resulted in a slightly more uniform cell distribution in the interstitial space. Spatiotemporal maps indicated that although both healthy and hardened cells tend to occasionally cross the centreline and enter the cell-depleted regions, the effect was more pronounced with hardened cells. Despite the sporadic cell crossing of these regions, there was no significant momentum transfer across the centreline; on average, there was negligible mixing between the two RBC streams within the short length of the interstitial space and hence the flow remained 'partitioned' for both healthy and hardened cells.

The present work illustrates the complex interplay between flow geometry and the particulate nature of blood. The non-uniform shear fields induced by the pillars and wall confinement give rise to heterogeneous cell distributions as reported in our previous study [1]. Changes in RBC deformability appear to manifest more in the spatiotemporal organisation of cells rather than velocities, which highlights the challenges in accurately modelling these flows. The study extends our previous work in bifurcating RBC flows [23,25,48] and complements efforts to understand flow partitioning in sequential bifurcations involving converging and diverging flows as in the present array.

Ethics approval

For the present work, Ethics Approval was obtained approved by the South East London NHS Research Ethics Committee (Reference: 10/H0804/21). Informed consent was obtained from all human participants.

Declaration of Competing Interest

The authors declare no conflicts of interest.

Acknowledgments

The support by the EPSRC DTP programme (EP/R513143/1) is gratefully acknowledged. The authors would like to thank Professor Gabriele Dubini and his team (Politecnico di Milano), particularly Dr. R. Gomez Bardon, for providing the microfluidic channels and the opportunity to study this configuration as part of their VPH CaSE project (www.vph-case.eu).

References

[1] Gómez Bardón R, Passos A, Piergiovanni M, Balabani S, Pennati G, Dubini G. Haematocrit heterogeneity in blood flows past microfluidic models of oxygenating fibre bundles. Med Eng Phys 2019;73:30–8. https://doi.org/10.1016/j.medengphy.2019.07.012.
[2] Pivkin IV, Peng Z, Karniadakis GE, Buffet PA, Dao M, Suresh S. Biomechanics of red blood cells in human spleen and consequences for physiology and disease. Proc Natl Acad Sci U S A 2016;113:7804–9. https://doi.org/10.1073/pnas.1606751113.
[3] Goldsmith HL. Red cell motions and wall interactions in tube flow. Fed Proc 1971;30:1578–90.
[4] Grandchamp X, Coupier G, Srivastav A, Minetti C, Podgorski T. Lift and down-gradient shear-induced diffusion in red blood cell suspensions. Phys Rev Lett 2013;110:108101. https://doi.org/10.1103/PhysRevLett.110.108101.
[5] Pranay P, Henríquez-Rivera RG, Graham MD. Depletion layer formation in suspensions of elastic capsules in Newtonian and viscoelastic fluids. Phys Fluids 2012;24:061902. https://doi.org/10.1063/1.4726058.
[6] Fenton BM, Carr RT, Cokelet GR. Nonuniform red cell distribution in 20 to 100μm bifurcations. Microvasc Res 1985;29:103–26. https://doi.org/10.1016/0026-2862(85)90010-X.
[7] Yen RT, Fung YC. Effect of velocity distribution on red cell distribution in capillary blood vessels. Am J Physiol Circ Physiol 1978;235:H251–7. https://doi.org/10.1152/ajpheart.1978.235.2.H251.
[8] Glenister FK, Coppel RL, Cowman AF, Mohandas N, Cooke BM. Contribution of parasite proteins to altered mechanical properties of malaria-infected red blood cells. Blood 2002;99:1060–3. https://doi.org/10.1182/blood.V99.3.1060.
[9] Alapan Y, Little JA, Gurkan UA. Heterogeneous red blood cell adhesion and deformability in sickle cell disease. Sci Rep 2014;4. https://doi.org/10.1038/srep07173.
[10] Tsukada K, Sekizuka E, Oshio C, Minamitani H. Direct measurement of erythrocyte deformability in diabetes mellitus with a transparent microchannel capillary model and high-speed video camera system. Microvasc Res 2001;61:231–9. https://doi.org/10.1006/mvre.2001.2307.
[11] Piagnerelli M, Boudjeltia KZ, Vanhaeverbeek M, Vincent J-L. Red blood cell rheology in sepsis. Intensive Care Med 2003;29:1052–61. https://doi.org/10.1007/s00134-003-1783-2.
[12] Bateman RM, Sharpe MD, Singer M, Ellis CG. The effect of sepsis on the erythrocyte. Int J Mol Sci 2017;18. https://doi.org/10.3390/ijms18091932.
[13] Lipowski HH. Microvascular rheology and hemodynamics. Microcirculation 2005;12:5–15. https://doi.org/10.1080/10739680590894966.
[14] Guizouarn H, Barshtein G. Editorial: red blood cell vascular adhesion and deformability. Front Physiol 2020;11:657. https://doi.org/10.3389/fphys.2020.00657.
[15] Alaarg A, Schiffelers RM, van Solinge WW, van Wijk R. Red blood cell vesiculation in hereditary hemolytic anemia. Front Physiol 2013;4:365. https://doi.org/10.3389/fphys.2013.00365.
[16] Huisjes R, Bogdanova A, van Solinge WW, Schiffelers RM, Kaestner L, van Wijk R. Squeezing for life – properties of red blood cell deformability. Front Physiol 2018;9:656. https://doi.org/10.3389/fphys.2018.00656.
[17] Kang YJ, Lee S-J. In vitro and ex vivo measurement of the biophysical properties of blood using microfluidic platforms and animal models. Analyst 2018;143:2723–49. https://doi.org/10.1039/C8AN00231B.
[18] Urbanska M, Muñoz HE, Shaw Bagnall J, Otto O, Manalis SR, Di Carlo D, et al. A comparison of microfluidic methods for high-throughput cell deformability measurements. Nat Methods 2020;17:587–93. https://doi.org/10.1038/s41592-020-0818-8.
[19] Guo Q, Reiling SJ, Rohrbach P, Ma H. Microfluidic biomechanical assay for red blood cells parasitized by Plasmodium falciparum. Lab Chip 2012;12:1143. https://doi.org/10.1039/c2lc20857a.
[20] Lanotte L, Mauer J, Mendez S, Fedosov DA, Fromental J-M, Claveria V, et al. Red cells' dynamic morphologies govern blood shear thinning under microcirculatory flow conditions. Proc Natl Acad Sci 2016;113:13289–94. https://doi.org/10.1073/pnas.1608074113.
[21] Faustino V, Rodrigues RO, Pinho D, Costa E, Santos-Silva A, Miranda V, et al. A microfluidic deformability assessment of pathological red blood cells flowing in a hyperbolic converging microchannel. Micromachines (Basel) 2019;10:645. https://doi.org/10.3390/mi10100645.
[22] Passos A, Sherwood JM, Kaliviotis E, Agrawal R, Pavesio C, Balabani S. The effect of deformability on the microscale flow behavior of red blood cell suspensions. Phys Fluids 2019;31:91903. https://doi.org/10.1063/1.5111189.
[23] Sherwood JM, Holmes D, Kaliviotis E, Balabani S. Spatial distributions of red blood cells significantly alter local haemodynamics. PLoS ONE 2014;9:e100473. https://doi.org/10.1371/journal.pone.0100473.

[24] Kaliviotis E, Pasias D, Sherwood JM, Balabani S. Red blood cell aggregate flux in a bifurcating microchannel. Med Eng Phys 2017;48:23–30. https://doi.org/10.1016/j.medengphy.2017.04.007.

[25] Sherwood JM, Dusting J, Kaliviotis E, Balabani S. The effect of red blood cell aggregation on velocity and cell-depleted layer characteristics of blood in a bifurcating microchannel. Biomicrofluidics 2012;6:024119. https://doi.org/10.1063/1.4717755.

[26] Reinhart WH, Piety NZ, Shevkoplyas SS. Influence of feeding hematocrit and perfusion pressure on hematocrit reduction (Fåhræus effect) in an artificial microvascular network. Microcirculation 2017;24:e12396. https://doi.org/10.1111/micc.12396.

[27] Fenech M, Girod V, Claveria V, Meance S, Abkarian M, Charlot B. Microfluidic blood vasculature replicas using backside lithography. Lab Chip 2019;19:2096–106. https://doi.org/10.1039/c9lc00254e.

[28] Fontanella AN, Schroeder T, Hochman DW, Chen RE, Hanna G, Haglund MM, et al. Quantitative mapping of hemodynamics in the lung, brain, and dorsal window chamber-grown tumors using a novel, automated algorithm. Microcirculation 2013;20:724–35. https://doi.org/10.1111/micc.12072.

[29] Kloosterman A, Hierck B, Westerweel J, Poelma C. Quantification of blood flow and topology in developing vascular networks. PLoS ONE 2014;9:e96856. https://doi.org/10.1371/journal.pone.0096856.

[30] Kelch ID, Bogle G, Sands GB, Phillips ARJ, Legrice IJ, Rod Dunbar P. Organ-wide 3D-imaging and topological analysis of the continuous microvascular network in a murine lymph node. Sci Rep 2015;5:1–19. https://doi.org/10.1038/srep16534.

[31] Huh D, Matthews BD, Mammoto A, Montoya-Zavala M, Hsin HY, Ingber DE. Reconstituting organ-level lung functions on a chip. Science 2010;328(80):1662–8. https://doi.org/10.1126/science.1188302.

[32] Mühlfeld C, Weibel ER, Hahn U, Kummer W, Nyengaard JR, Ochs M. Is length an appropriate estimator to characterize pulmonary alveolar capillaries? A critical evaluation in the human lung. Anat Rec 2010;293:1270–5. https://doi.org/10.1002/ar.21158.

[33] Huang D, Liu T, Liao J, Maharjan S, Xie X, Pérez M, et al. Reversed-engineered human alveolar lung-on-a-chip model. Proc Natl Acad Sci 2021;118:e2016146118. https://doi.org/10.1073/pnas.2016146118.

[34] Chernyavsky IL, Jensen OE, Leach L. A mathematical model of intervillous blood flow in the human placentone. Placenta 2010;31:44–52. https://doi.org/10.1016/j.placenta.2009.11.003.

[35] Gill JS, Salafia CM, Grebenkov D, Vvedensky DD. Modeling oxygen transport in human placental terminal villi. J Theor Biol 2011;291:33–41. https://doi.org/10.1016/j.jtbi.2011.09.008.

[36] Holmes D, Whyte G, Bailey J, Vergara-Irigaray N, Ekpenyong A, Guck J, et al. Separation of blood cells with differing deformability using deterministic lateral displacement. Interface Focus 2014;4:20140011. https://doi.org/10.1098/rsfs.2014.0011.

[37] Guo Q, Duffy SP, Matthews K, Deng X, Santoso AT, Islamzada E, et al. Deformability based sorting of red blood cells improves diagnostic sensitivity for malaria caused by plasmodium falciparum. Lab Chip 2016;16:645–54. https://doi.org/10.1039/C5LC01248A.

[38] Kang YJ, Ha Y-R, Lee S-J. Deformability measurement of red blood cells using a microfluidic channel array and an air cavity in a driving syringe with high throughput and precise detection of subpopulations. Analyst 2016;141:319–30. https://doi.org/10.1039/C5AN01988E.

[39] Choi J, Hyun J, Yang S. On-chip extraction of intracellular molecules in white blood cells from whole blood. Sci Rep 2015;5:15167. https://doi.org/10.1038/srep15167.

[40] Stauber H, Waisman D, Korin N, Sznitman J. Red blood cell dynamics in biomimetic microfluidic networks of pulmonary alveolar capillaries. Biomicrofluidics 2017;11:014103. https://doi.org/10.1063/1.4973930.

[41] Rigat-Brugarolas LG, Elizalde-Torrent A, Bernabeu M, De Niz M, Martin-Jaular L, Fernandez-Becerra C, et al. A functional microengineered model of the human splenon-on-a-chip. Lab Chip 2014;14:1715–24. https://doi.org/10.1039/C3LC51449H.

[42] Elizalde-Torrent A, Trejo-Soto C, Méndez-Mora L, Nicolau M, Ezama O, Gualdrón-López M, et al. Pitting of malaria parasites in microfluidic devices mimicking spleen interendothelial slits. Sci Rep 2021;11:22099. https://doi.org/10.1038/s41598-021-01568-w.

[43] Serov AS, Salafia CM, Brownbill P, Grebenkov DS, Filoche M. Optimal villi density for maximal oxygen uptake in the human placenta. J Theor Biol 2015;364:383–96. https://doi.org/10.1016/j.jtbi.2014.09.022.

[44] Jensen OE, Chernyavsky IL. Annual review of fluid mechanics blood flow and transport in the human placenta. Annu Rev Fluid Mech 2019;51:25–47. https://doi.org/10.1146/annurev-fluid-010518.

[45] Krüger T, Holmes D, Coveney PV. Deformability-based red blood cell separation in deterministic lateral displacement devices—A simulation study. Biomicrofluidics 2014;8:054114. https://doi.org/10.1063/1.4897913.

[46] Wang T, Rongin U, Xing Z. A micro-scale simulation of red blood cell passage through symmetric and asymmetric bifurcated vessels. Sci Rep 2016;6:20262. https://doi.org/10.1038/srep20262.

[47] Zhang Z, Henry E, Gompper G, Fedosov DA. Behavior of rigid and deformable particles in deterministic lateral displacement devices with different post shapes. J Chem Phys 2015;143:243145. https://doi.org/10.1063/1.4937171.

[48] van Batenburg-Sherwood J, Balabani S. Continuum microhaemodynamics modelling using inverse rheology. Biomech Model Mechanobiol 2021:1–27. https://doi.org/10.1007/s10237-021-01537-2.

[49] Thielicke W, Stamhuis EJ. PIVlab – towards user-friendly, affordable and accurate digital particle image velocimetry in MATLAB. J Open Res Softw 2014;2. https://doi.org/10.5334/jors.bl.

[50] Westerweel J, Scarano F. Universal outlier detection for PIV data. Exp Fluids 2005;39:1096–100. https://doi.org/10.1007/s00348-005-0016-6.

[51] Olsen MG, Adrian RJ. Out-of-focus effects on particle image visibility and correlation in microscopic particle image velocimetry. Exp Fluids 2000;29:S166–74. https://doi.org/10.1007/s003480070018.

[52] Poelma C, Kloosterman A, Hierck BP, Westerweel J. Accurate blood flow measurements: are artificial tracers necessary? PLoS ONE 2012;7:45247. https://doi.org/10.1371/journal.pone.0045247.

[53] Sherwood JM, Kaliviotis E, Dusting J, Hematocrit Balabani S. Viscosity and velocity distributions of aggregating and non-aggregating blood in a bifurcating microchannel. Biomech Model Mechanobiol 2014;13:259–73. https://doi.org/10.1007/s10237-012-0449-9.

[54] Cagney N, Lacassagne T, Balabani S. Taylor-Couette flow of polymer solutions with shear-thinning and viscoelastic rheology. J Fluid Mech 2020;905:A28. https://doi.org/10.1017/jfm.2020.701.

[55] Abay A, Recktenwald SM, John T, Kaestner L, Wagner C-T. Cross-sectional focusing of red blood cells in a constricted microfluidic channel. Soft Matter 2020;16:534–43. https://doi.org/10.1039/C9SM01740B.

[56] Zhou Q, Fidalgo J, Calvi L, Bernabeu MO, Hoskins PR, Oliveira MSN, et al. Spatiotemporal dynamics of dilute red blood cell suspensions in low-inertia microchannel flow. Biophys J 2020;118:2561–73. https://doi.org/10.1016/j.bpj.2020.03.019.

[57] Mantegazza A, Clavica F, Obrist D. In vitro investigations of red blood cell phase separation in a complex microchannel network. Biomicrofluidics 2020;14:14101. https://doi.org/10.1063/1.5127840.

[58] Losserand S, Coupier G, Podgorski T. Migration velocity of red blood cells in microchannels. Microvasc Res 2019;124:30–6. https://doi.org/10.1016/j.mvr.2019.02.003.

[59] Schmid F, Barrett MJP, Obrist D, Weber B, Jenny P. Red blood cells stabilize flow in brain microvascular networks. PLOS Comput Biol 2019;15:e1007231. https://doi.org/10.1371/journal.pcbi.1007231.

[60] Mantegazza A, Ungari M, Clavica F, Obrist D. Local vs. global blood flow modulation in artificial microvascular networks: effects on red blood cell distribution and partitioning. Front Physiol 2020;11:566273. https://doi.org/10.3389/fphys.2020.566273.

[61] Chen Y, Li D, Li Y, Wan J, Li J, Chen H. Margination of stiffened red blood cells regulated by vessel geometry. Sci Rep 2017;7:15253. https://doi.org/10.1038/s41598-017-15524-0.

[62] Olla P. The role of tank-treading motions in the transverse migration of a spheroidal vesicle in a shear flow. J Phys A Math Gen 1997;30:317–29. https://doi.org/10.1088/0305-4470/30/1/022.

[63] Dupire J, Socol M, Viallat A. Full dynamics of a red blood cell in shear flow. Proc Natl Acad Sci 2012;109:20808–13. https://doi.org/10.1073/pnas.1210236109.

[64] Hariprasad DS, Secomb TW. Two-dimensional simulation of red blood cell motion near a wall under a lateral force. Phys Rev E 2014;90:053014. https://doi.org/10.1103/PhysRevE.90.053014.

[65] Krüger T. Effect of tube diameter and capillary number on platelet margination and near-wall dynamics. Rheol Acta 2016;55:511–26. https://doi.org/10.1007/s00397-015-0891-6.

[66] Forsyth AM, Wan J, Ristenpart WD, Stone HA. The dynamic behavior of chemically "stiffened" red blood cells in microchannel flows. Microvasc Res 2010;80:37–43. https://doi.org/10.1016/j.mvr.2010.03.008.

[67] Namgung B, Ng YC, Leo HL, Rifkind JM, Kim S. Near-wall migration dynamics of erythrocytes in vivo: effects of cell deformability and arteriolar bifurcation. Front Physiol 2017;8:1–10. https://doi.org/10.3389/fphys.2017.00963.

[68] Kumar A, Graham MD. Margination and segregation in confined flows of blood and other multicomponent suspensions. Soft Matter 2012;8:10536. https://doi.org/10.1039/c2sm25943e.

[69] Závodszky G, Van Rooij B, Czaja B, Azizi V, De Kanter D, Hoekstra AG. Red blood cell and platelet diffusivity and margination in the presence of cross-stream gradients in blood flows. Phys Fluids 2019;31:31903. https://doi.org/10.1063/1.5085881.

[70] Czaja B, Gutierrez M, Závodszky G, De Kanter D, Hoekstra A, Eniola-Adefeso O. The influence of red blood cell deformability on hematocrit profiles and platelet margination. PLoS Comput Biol 2020;16:e1007716. https://doi.org/10.1371/journal.pcbi.1007716.

[71] Loiseau E, Massiera G, Mendez S, Martinez PA, Abkarian M. Microfluidic study of enhanced deposition of sickle cells at acute corners. Biophys J 2015;108:2623–32. https://doi.org/10.1016/j.bpj.2015.04.018.

[72] Henríquez Rivera RG, Zhang X, Graham MD. Mechanistic theory of margination and flow-induced segregation in confined multicomponent suspensions: simple shear and Poiseuille flows. Phys Rev Fluids 2016;1:060501. https://doi.org/10.1103/PhysRevFluids.1.060501.

[73] Balabani S, Yianneskis M. An experimental study of the mean flow and turbulence structure of cross-flow over tube bundles. Proc Inst Mech Eng Part C J Mech Eng Sci 1996;210:317–31. https://doi.org/10.1243/PIME_PROC_1996_210_204_02.

[74] Konstantinidis E, Castiglia D, Balabani S, Yianneskis M. On the flow and vortex shedding characteristics of an in-line tube bundle in steady and pulsating crossflow. Chem Eng Res Des 2000;78:1129–38. https://doi.org/10.1205/026387600528283.